Structural stability, dynamical stability, thermoelectric properties, and elastic properties of GeTe at high pressure

Hardik L. Kagdada,[1] Prafulla K. Jha,[1,*] Piotr Śpiewak,[2] and Krzysztof J. Kurzydłowski[2]

[1]*Department of Physics, Faculty of Science, The Maharaja Sayajirao University of Baroda, Vadodara-390002, India*

[2]*Materials Design Division, Faculty of Materials Science and Engineering, Warsaw University of Technology, 141 Wołoska Str., 02–507 Warsaw, Poland*

The stability of GeTe in rhombohedral ($R3m$), face centred cubic ($Fm3m$), and simple cubic ($Pm3m$) phases has been studied using density functional perturbation theory. The rhombohedral phase of GeTe is dynamically stable at 0 GPa, while $Fm3m$ and $Pm3m$ phases are stable at 3.1 and 33 GPa, respectively. The pressure-dependent phonon modes are observed in $Fm3m$ and $Pm3m$ phases at Γ and M points, respectively. The electronic and the thermoelectric properties have been investigated for the stable phases of GeTe. The electronic band gap for rhombohedral and $Fm3m$ phases of GeTe has been observed as 0.66 and 0.17 eV, respectively, while the $Pm3m$ phase shows metallic behavior. We have used the Boltzmann transport equation under a rigid band approximation and constant relaxation time approximation as implemented in BOLTZTRAP code for the calculation of thermoelectric properties of GeTe. The metallic behavior of $Pm3m$ phase gives a very low value of Seebeck coefficient compared to the other two phases as a function of temperature and the chemical potential μ. It is observed that the rhombohedral phase of GeTe exhibits higher thermoelectric performance. Due to the metallic nature of $Pm3m$ phase, negligible thermoelectric performance is observed compared to $R3m$ and $Fm3m$-GeTe. The calculated lattice thermal conductivities are low for $Fm3m$-GeTe and high for $R3m$-GeTe. At the relatively higher temperature of 1350 K, the figure of merit ZT is found to be 0.7 for rhombohedral GeTe. The elastic constants satisfy the Born stability criteria for all three phases. The rhombohedral and $Fm3m$ phases exhibits brittleness and the $Pm3m$ phase shows ductile nature.

I. INTRODUCTION

In recent years, chalcogenide compounds have received much more attention by the condensed matter and materials researchers due to their complex sequence of structural phase transitions and excellent properties such as ferroelectricity, superconductivity, and high thermoelectric power resulting in a variety of applications mainly in storage devices, industrial perspectives, and thermoelectric devices [1–6]. Among these materials, germanium (Ge), tin (Sn), and lead (Pb) based tellurides and selenides are studied significantly due to their complex and interesting structural phase transition sequences at high pressure and thermoelectric properties [7–11]. The binary chalcogenides such as lead-, tin-, and germanium-based tellurides exhibit a pressure induced structural phase transition from face centered cubic ($Fm3m$) to simple cubic ($Pm3m$) structure at high pressure [12–16]. In addition, there appears an intermediate phase between $Fm3m$ and CsCl-type structures [9,12–15]. GeTe, which crystallizes in rhombohedral ($R3m$) structure at ambient conditions with displaced ionic positions of rock-salt sites, exhibits a temperature-dependent structural phase transition from ground-state $R3m$ to $Fm3m$ structure at 720 K [17,18]. This transition occurs without any change in the number of atoms per unit cell, but the symmetry of the structure changes from lower to higher-symmetry structure

with increasing temperature, which is attributed to the second-order phase transition [18]. However, under pressure, the phase transition from $R3m$ to $Fm3m$ phase is a first-order transition as evidenced by the volume discontinuity at 3.1 GPa [18]. Furthermore, GeTe exhibits paraelectric nature with the $Fm3m$ phase above the transition temperature, while below the transition temperature it shows ferroelectricity with displaced atomic positions from its ideal rock-salt sites [19]. This transition is derived by a temperature- dependent soft phonon mode observed at 140 cm^{-1} in the $R3m$ phase [19]. The structural phase transition in GeTe with increasing temperature is due to softening of A$_1$ and E phonon modes, which abolishes the rhombohedral angular distortion of 1.8° above the transition temperature, 705 K [6,20,21]. Onodera *et al.* [22] found a transition from $R3m$ to $Fm3m$ structure around 3 GPa without any volume discontinuity followed by another transition to an orthorhombic phase with a $Pbcn$ space group at 18 GPa. *Ab initio* calculations of the pressure induced structural phase transitions of GeTe by Do *et al.* [7] show an $Fm3m$ to $Pm3m$ transformation at 42.9 GPa. Very recently, Jeong *et al.* [23] reported the coexistence of $R3m$, Cm, and $P1$ phases in crystalline GeTe from the change in internal energy. They further found that the structural phase transformation induces the change in crystal resistance.

Tellurides including GeTe have been the focused materials for thermoelectric applications in the last few years [7,10,24,25]. GeTe exhibits remarkable thermoelectric performance with alloying of PbTe and doping of Sb$_2$Te$_3$, which

---

*prafullaj@yahoo.com; pk.jha-phy@msubaroda.ac.in

reduces the carrier concentration and lattice thermal conductivity [26]. Very recently, large number of GeTe samples with a wide range of carrier concentrations have been synthesized, and first-principles based electronic band structure calculations show that the thermoelectric performance is better for GeTe compared to PbTe and SnTe due to the highly degenerated Σ band at the band edge [27]. The study of Lanqing *et al.* [10] of the thermoelectric properties of GeTe with $Fm3m$ phase for both p and n type shows a quick drop at high pressure in contrast to a high thermoelectric performance at zero pressure. This clearly brings out the importance of pressure and pressure induced structural phase transitions in tellurides, particularly in GeTe. Here, our aim is to study the dynamical stability, elastic properties, and electronic and thermal transport properties of GeTe under pressure.

II. COMPUTATIONAL METHOD

The structural, electronic, and elastic properties of GeTe in different phases with pressure variation are investigated using first-principles calculations in the framework of density functional theory (DFT) implemented in QUANTUM ESPRESSO code [28]. The ground-state optimization of all the structures is performed using the Broyden-Fletcher-Goldfarb-Shanno (BFGS) method [29–32]. Both cell parameters and atomic coordinates are optimized at each pressure [33]. The norm conserving type pseudopotential with generalized gradient approximation (GGA) proposed by Perdew-Burke-Ernzerhof (PBE) was employed for the exchange correlation functional [34]. The plane-wave basis set cutoff energy for $R3m$ and $Pm3m$ phases is 100 Ry and for the $Fm3m$ phase it is 90 Ry. The Brillouin zone integration was performed with a $12 \times 12 \times 12$ k mesh for $Fm3m$ and $Pm3m$ phases, while for the $R3m$ structure we used a $14 \times 14 \times 14$ k mesh within the Monkhorst-Pack scheme. The iterative Davidson-type diagonalization method is used to solve the Kohn–Sham equation with energy convergence threshold of 1×10^{-7} Ry. We have treated the $4d$ orbitals as valence states in generating pseudopotentials [35,36]. The phonon properties were computed using the density functional perturbation theory (DFPT), which allows us to calculate the phonons at any wave vector in the unit cell that is implemented in QUANTUM ESPRESSO code [37]. To calculate the dynamical matrix at each $\mathbf{q}$ grid, we have used a $6 \times 6 \times 6$ q mesh for the $Fm3m$ phase, while for $R3m$ and $Pm3m$ phases we used a $4 \times 4 \times 4$ q mesh. The Boltzmann transport equation is used to calculate thermoelectric properties under the constant relaxation time approximation (CRTA) implemented in BOLTZTRAP code [38]. This equation together with the *ab initio* approach has been quite successful in predicting the transport properties of a variety of compounds and potential thermoelectric (TE) materials [39,40]. In the case of CRTA, the required relaxation time τ is treated as constant, which results into the determination of Seebeck coefficient S and electrical conductivity relative to the relaxation time σ/τ without any fitting parameter. However, the electrical conductivity σ and hence the power factor $S^2\sigma$ and ZT can be resolved with respect to τ. The thermoelectric properties can be estimated by considering the rigid band approximation in the calculation of the electronic band structure. Furthermore, for a direct comparison with measured data, determination

of the carrier concentration from the temperature-dependent chemical potential is needed. The temperature dependence of the chemical potential (μ) can be expressed as

$$n = \int D_e(E) \frac{1}{e^{\frac{(\mu - E)}{k_B T}} + 1} dE, \qquad (1)$$

where n, E, $D_e(E)$, k_B, and T are the carrier concentration, energy, density of states, Boltzmann's constant, and temperature, respectively. The lattice thermal conductivity is obtained using the phonon Boltzmann transport equation (PBTE) and SHENGBTE code [41]. The lattice thermal conductivity at a temperature T can be expressed as

$$\kappa_{\text{latt}} = \frac{1}{NV} \sum_\lambda \frac{\partial f}{\partial T(\hbar \omega_\lambda)} v_\lambda^\alpha v_\lambda^\alpha \tau_\lambda, \qquad (2)$$

where N, V, f, and v_λ^α are the number of uniformly shaped $\mathbf{q}$ points in the Brillouin zone (BZ), volume of the unit cell, the Boltzmann distribution function and velocity along α direction. To solve the PBTE, harmonic force constants (second-order) and anharmonic (third-order) force constants (IFCs) are required to calculate the lattice thermal conductivity. We used DFPT in order to calculate second-order force constants, while third-order anharmonic force constants (IFCs) are calculated with a supercell of $3 \times 3 \times 3$. Analysis of mechanical properties for all three phases has been done by calculating elastic constants (C_{ij}), bulk modulus (B), shear modulus (G), and Young's modulus (Y), Poisson's coefficient (η), and anisotropic factor A. For this, we first generate a set of distorted structures by applying Lagrangian strain of 0.15 on the relaxed structures using ELASTIC code [42]. For each deformed structure, the full stress tensor is calculated by relaxation of ions using DFT and then is used to calculate the elastic properties. Using elastic constants, we calculated the elastic moduli by adopting the Voigt-Reuss-Hill approximation [43].

III. RESULTS AND DISCUSSION

A. Crystal structures

GeTe consists of several structures from rhombohedral to simple cubic ($Pm3m$) with different space groups at different pressure and temperature. The ground-state phase of GeTe is rhombohedral ($R3m$) and it transforms into face centered cubic phase with $Fm3m$ space group at 3.5 GPa [44]. To reach a final $Pm3m$ phase from cubic $Fm3m$, there are mainly three ways as shown schematically in Fig. 1. The first path known as Watanabe path (top most) is through the orthorhombic phase with $Pmmn$ space group, which is transformed from $Fm3m$ at 34.5 GPa and then finally to $Pm3m$ phase at 48.8 GPa [7]. The other paths Tolendo and modified Buerger are the transformation from $Fm3m$ phase to $Pbnm$ phase at 19.2 GPa and $P2_1/m$ phase at 18.6 GPa, respectively, and then to metastable orthorhombic ($Cmcm$ space group) structure followed by another transformation to $Pm3m$ at pressure greater than 50 GPa [7,16]. The fourth path is the direct transformation from $Fm3m$ to $Pm3m$. Serebryanaya *et al.* [16] obtained a CsCl-type structure with $Pm3m$ space group for GeTe at 38 GPa with a lattice constant $a = 3.268$ Å. In the present study, we choose the third path, in which GeTe transforms directly from $Fm3m$ to $Pm3m$ structure without
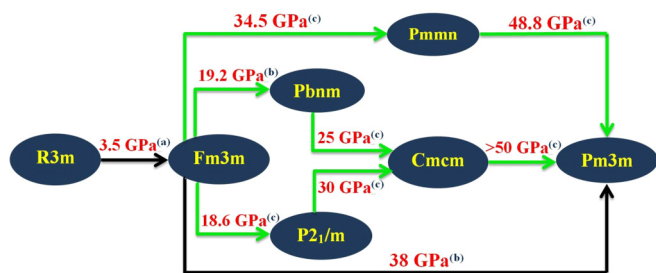
FIG. 1. Different transition paths for GeTe from $R3m$ to $Pm3m$ with pressure. We take the $R3m \to Fm3m \to Pm3m$ path, which is indicated by a black color line. Other paths are based on literature survey: (a) Ref. [44], (b) Ref. [16], and (c) Ref. [7].

FIG. 2. Unit cell of GeTe (a) rhombohedral, (b) $Fm3m$, and (c) $Pm3m$ phases. The rhombohedral phase has an angle of 58.264°. Blue color represents Ge and red color represents Te atoms.

any intermediate structure. We consider three structures of GeTe: (i) rhombohedral ($R3m$), (ii) FCC ($Fm3m$), and (iii) SC ($Pm3m$), and calculate the minimum energy of each structure. For better clarity of some of the states, we provide the structures together with the lattice parameters in Fig. S1 of Ref. [45]. The stability of the considered phase is discussed in the next section. The rhombohedral structure of GeTe consists of various structural discrepancies. The experimental study by Pereira *et al.* shows that the $R3m$ phase with $a = 4.156$ Å and $c = 10.663$ Å at room temperature that can convert into the rhombohedral structure with lattice constant $a = 4.288$ Å and angle $\alpha = 57.93°$, which are in close agreement with our calculated structural parameters for the $R3m$ phase [46]. Our optimized lattice parameters for the ground-state rhombohedral phase presented in Table I are in good agreement with the experimentally reported structural parameters of GeTe [47,48]. Figure S2 of Ref. [45] presents the plot of $E(V)$ for three considered phases. The volume change in $R3m$ and $Fm3m$ phases is found almost of the same order, which depicts the first-order structural phase transition from $R3m$ to $Fm3m$
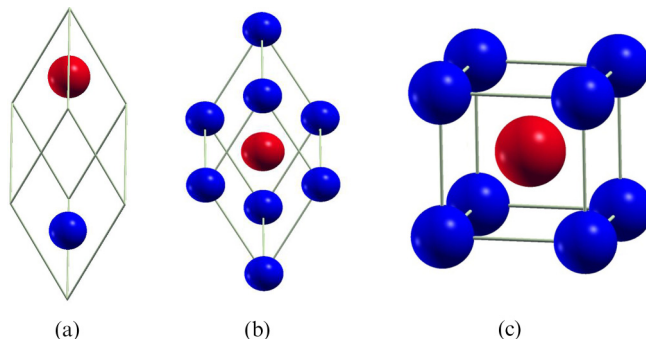
phase. Figure 2 presents the unit cell of GeTe in all three phases, $R3m$, $Fm3m$, and $Pm3m$. The atomic coordinates and interaxial angle in $R3m$ phase is listed in Table I, which agrees well with available reports.

B. Dynamical stability at high pressure

The lattice dynamics is important to understand the stability of phase, phase-transition, and electron-phonon interaction of a material. Furthermore, a good thermoelectric material should have low thermal conductivity as the thermoelectric figure of merit ZT is inversely proportional to it. The lattice thermal conductivity κ_{latt} is lower for low sound velocity and materials with soft lattices and weak elastic properties, which normally give low lying optical phonon modes in phonon dispersion curves [49]. This results into the anharmonic coupling between these optical phonon and acoustic phonons and therefore a strong scattering of acoustic phonon is induced [49,50]. In this section, we focus on the phonon properties and dynamical stability of GeTe in all three considered phases. The phonon dispersion

TABLE I. Our calculated and other theoretical and experimental lattice parameters and atomic positions of GeTe.

System	Work	a (Å)	Inter axial angle (°)		Atomic coordinates (crystal unit)		
					x	y	z
$R3m$	Present	4.323	58.264	Ge	0.2359	0.2359	0.2359
				Te	−0.2359	−0.2359	−0.2359
	Other	4.260[a], 4.33[b]	58.358[a], 58.14[b]	Ge[b]	0.2359	0.2359	0.2359
				Te[b]	−0.2359	−0.2359	−0.2359
$Fm3m$	Present	5.919	90	Ge	0.0	0.0	0.0
				Te	0.5	0.5	0.5
	Other	5.974[c], 5.986[d]	90	Ge[d]	0.0	0.0	0.0
				Te[d]	0.5	0.5	0.5
$Pm3m$	Present	3.283	90	Ge	0.0	0.0	0.0
				Te	0.5	0.5	0.5
	Other	3.270[e], 3.268[f]	90	Ge[f]	0.0	0.0	0.0
				Te[f]	0.5	0.5	0.5

[a]Reference [22].
[b]Reference [48].
[c]Reference [7].
[d]Reference [44].
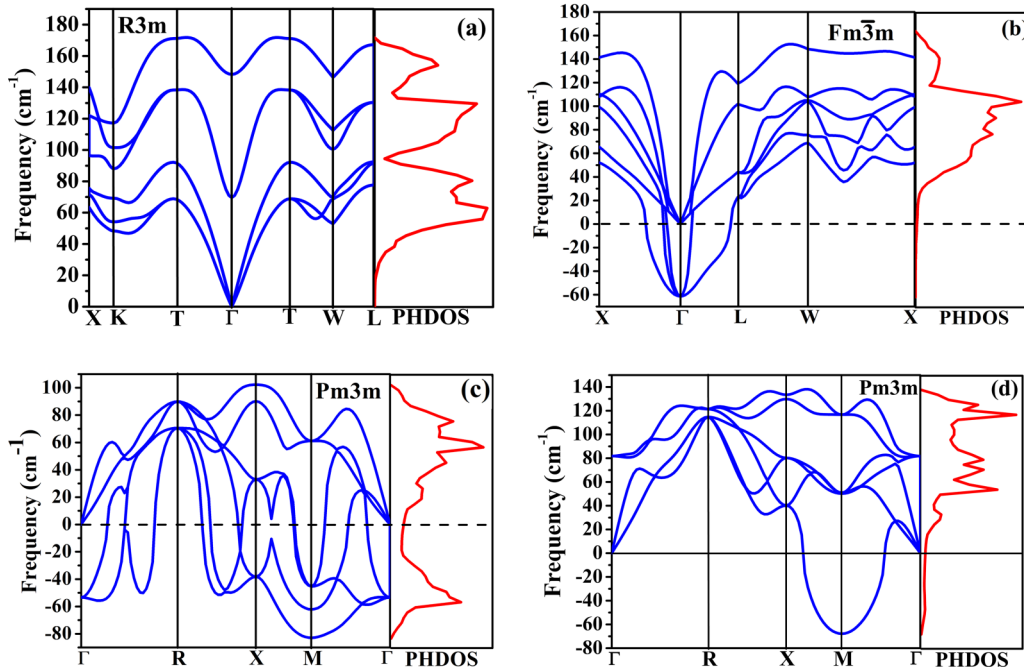[e]Reference [7].
[f]Reference [16].

FIG. 3. Phonon dispersion curves along high-symmetry directions and the phonon density of states (PHDOS) for GeTe in (a) $R3m$, (b) $Fm3m$, and (c) $Pm3m$ phases at 0 GPa. The negative PHDOS in $Fm3m$ and $Pm3m$ phases shows instability in GeTe at 0 GPa. (d) Phonon dispersion and PHDOS for $Pm3m$ phase at 10 GPa.

and phonon density of states (PHDOS) for $R3m$, $Fm3m$, and $Pm3m$ phases at 0 GPa are presented in Fig. 3. Since there are two atoms per unit cell for all three structures of GeTe, there are six phonon modes in phonon dispersion curves (PDC). The $R3m$ phase is dynamically stable at 0 GPa as no imaginary frequency of phonon modes is found in the entire BZ. There is a degeneracy in transverse acoustic (TA) and transverse optical (TO) modes in higher-symmetry directions of the BZ in the rhombohedral phase. However, in other phases such as $Fm3m$ and $Pm3m$, there exist imaginary eigenvalues in the BZ. While in the $Fm3m$ phase [Fig. 3(b)] the phonon modes with imaginary frequency exist only at zone center, in the case of $Pm3m$ phase, they are located at Γ, X, and M points of BZ. The $Fm3m$ and $Pm3m$ phases of GeTe, which are not observed at ambient conditions, depict the dynamically unstable structure at 0 GPa. A threefold degenerate infrared active mode T_{1u} is observed at Γ point with a maximum imaginary frequency of 64.1 cm^{-1} in the $Fm3m$ phase at 0 GPa. This threefold degenerated mode splits into degenerated two TO modes and one LO mode, which results into the LO-TO splitting along the Γ to L direction. In certain cases under pressure, the eigenvalues of the phonon modes turn real. In the present study, we have systematically, step by step applied pressure for the $Fm3m$ phase and calculated the PDC, which are presented in Fig. 4(a). The magnitude of the phonon frequency at Γ point decreases as the pressure increases and at 3.1 GPa the imaginary eigenvalues completely disappear [Fig. 4(b)]. The eigenvalues located at other points of BZ remain almost constant with pressure. This indicates that the $Fm3m$ phase, which was unstable at 0 GPa, becomes stable at 3.1 GPa, which is close to the experimental value of 3.5 GPa.

Figures 3(c) and 3(d) show the phonon dispersion along the Γ-R-X-M-Γ direction of BZ together with the phonon density

of states for the $Pm3m$ phase at two pressures, 0 and 10 GPa, respectively. It can be seen that the $Pm3m$ phase of GeTe is unstable at 0 GPa as the imaginary frequency is observed at high symmetry points Γ (0.0 0.0 0.0), X (0.0 0.5 0.0), and M (0.5 0.0 0.5) of the BZ. The imaginary frequency is maximum with 82 cm^{-1} at M point for 0 GPa. However, after applying pressure of 10 GPa, the phonon modes at Γ and X points turn real, while at M point one of the TA modes with B_{1u} symmetry still remains imaginary. However, with systematic application of pressure, similar to the $Fm3m$ phase the imaginary frequency of TA mode at M point turns real. Figure 4(c) presents the phonon dispersion of GeTe in the $Pm3m$ phase along the high-symmetry points X-M-Γ, which shows that the TA mode turns real with increasing pressure. At 33 GPa, the frequency of TA phonon modes at M point becomes real, indicating dynamical stability of GeTe in $Pm3m$ phase [Fig. 4(d)]. All properties presented in the next section are calculated for stable phases of GeTe.

C. Electronic and thermal transport properties

We now move to the electronic and thermoelectric properties of GeTe. We have calculated the electronic band structure together with the density of states (DOS) and thermoelectric coefficients for the stable configurations of GeTe, i.e., $R3m$-GeTe at 0 GPa, $Fm3m$-GeTe at 3.1 GPa, and $Pm3m$-GeTe at 33 GPa. The calculated electronic band structure and density of states for $R3m$, $Fm3m$, and $Pm3m$ structures at stable pressure are also shown in Fig. 5. It is found that the rhombohedral phase has the largest band gap of 0.66 eV, while $Fm3m$ has the lowest with 0.17 eV. The $Pm3m$ phase of GeTe shows no band gap, indicating metallic behavior. The nature of the band gap in the $R3m$ phase is direct at T (0.5, 0.0, 0.0)
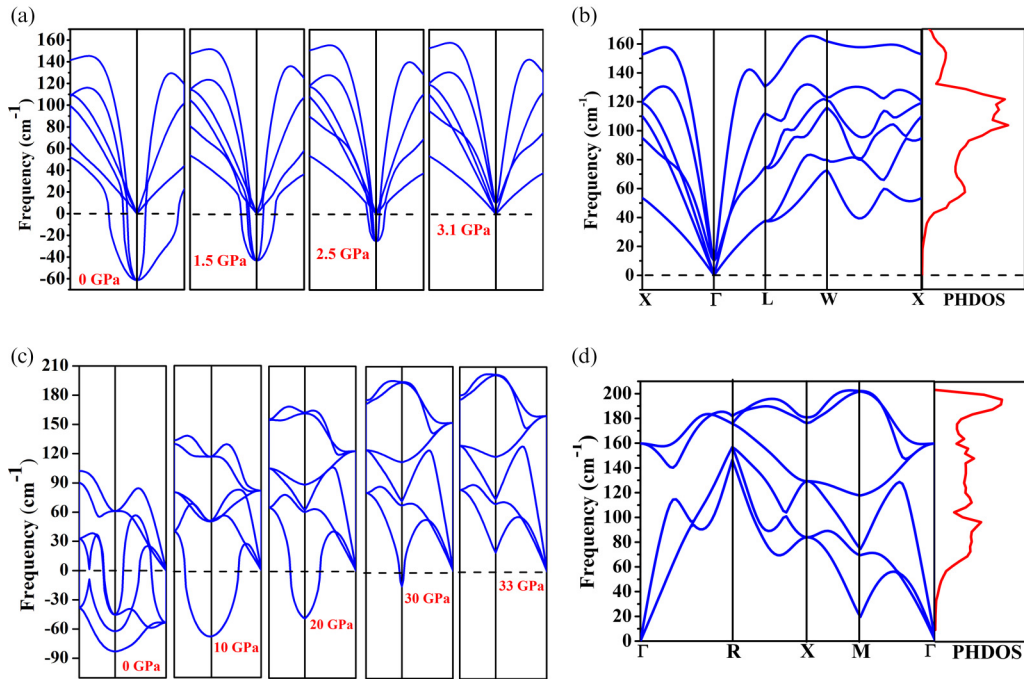
FIG. 4. Pressure-dependent phonon modes for (a) $Fm3m$ and (c) $Pm3m$ phases around Γ and M points, respectively. At 3.1 GPa, the imaginary mode of $Fm3m$ phase at Γ point disappeared and similarly at 33 GPa the phonon mode of $Pm3m$ phase at M point disappeared. The full phonon dispersion curves for $Fm3m$ at 3.1 GPa and $Pm3m$ at 33 GPa are shown in (b) and (d), respectively.

and L (0.5, 0.0, 0.0) points of the BZ, respectively, while in the $Fm3m$ phase it is direct at L point only. In the band structure of $R3m$, the higher-symmetry points L and T are equivalent; the difference is only in the location. The L point is located at the center of a hexagonal face, while the T point is located at a trigonal face in BZ [51]. The nature of
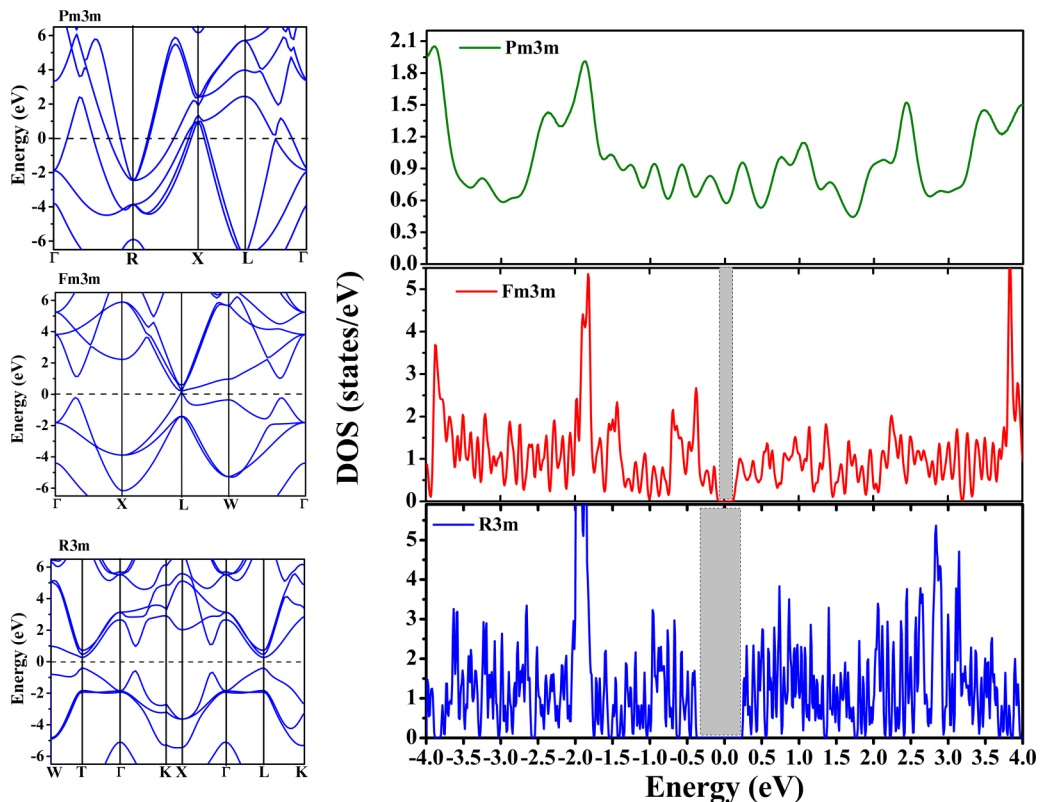

FIG. 5. Electronic band structure (left) and density of states (right) of $R3m$, $Fm3m$, and $Pm3m$ structures.
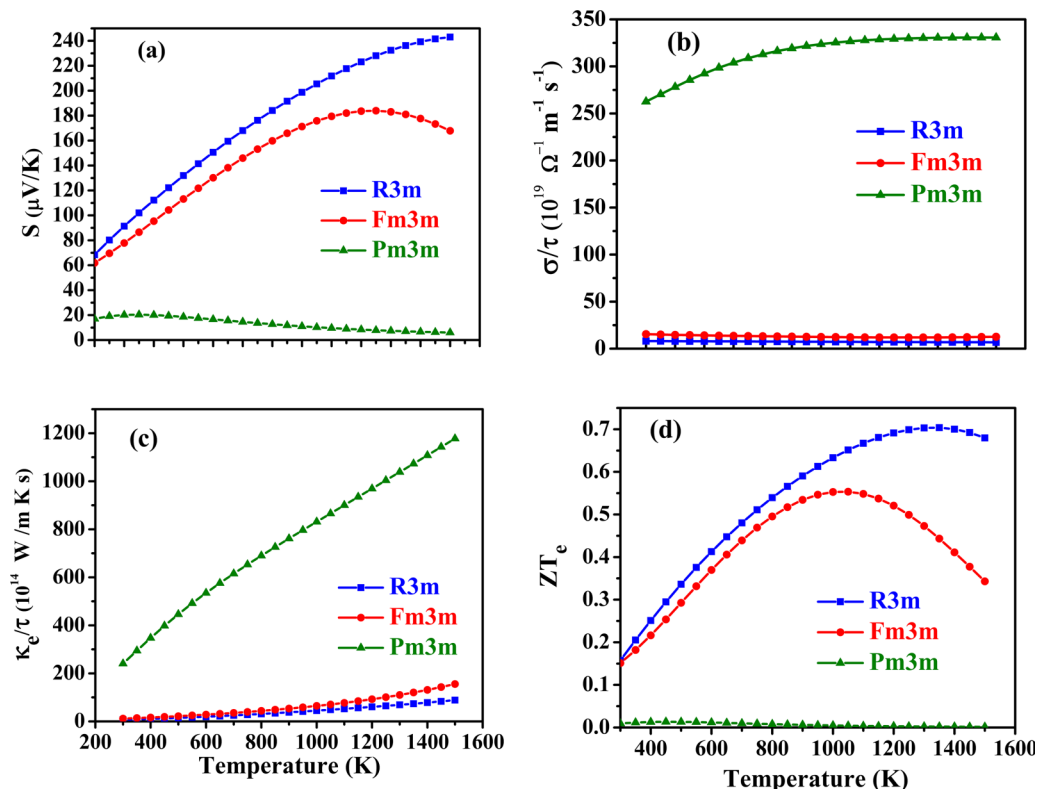
FIG. 6. Temperature-dependent thermoelectric parameters for all three phases: (a) Seebeck coefficient, (b) electrical conductivity, (c) electronic thermal conductivity, and (d) electronic thermoelectric figure of merit. The electrical conductivity and electronic thermal conductivity are calculated in terms of relaxation time.

the band structure is consistent with earlier reports [7,23,52]. Our calculated band gap value varies slightly from the earlier reported values [7,23,52], which can be attributed to the use of GGA for the electron exchange correlation interactions. The inclusion of GGA-PBE with DFT-D2 and hybrid functionals has been found to significantly enhance the band gap of $R3m$ and $Fm3m$ phases of GeTe [23] and others. The band gaps of $R3m$ and $Fm3m$ phases are higher than some conventional thermoelectric materials like Bi_2Te_3, which gives a greater enhancement in the Seebeck coefficient [53]. Figure 6 shows the temperature-dependent thermoelectric coefficients in the temperature range of 300 to 1500 K for stable phases of GeTe. We have assumed a series of carrier concentration ranging from 1×10^{18} to 9×10^{20} cm^{-1}. The Seebeck coefficient for $R3m$-GeTe with the carrier concentration of 7×10^{20} cm^{-1} is found to be 68 μV/K, which is in close agreement with the experimental value of 80 μV/K at 300 K [25]. Therefore we selected this carrier concentration for the calculation of other coefficients of transport properties. As shown in Fig. 6(a), the Seebeck coefficient, which increases with temperature, is highest for $R3m$-GeTe over the whole temperature range. The $R3m$-GeTe exhibits maximum value of Seebeck coefficient with 243.05 μV/K at 1500 K, while at the same temperature $Fm3m$-GeTe and $Pm3m$-GeTe have 167.90 and 5.99 μV/K, respectively. The significantly low value of Seebeck coefficient for $Pm3m$-GeTe is attributed to its metallic nature. The Seebeck coefficient is independent of relaxation time τ, but the τ dependency of electrical conductivity σ can be expressed by

the following expression:

$$\sigma = \frac{ne^2 m^*}{\tau}, \qquad (3)$$

where n is the carrier concentration, e is the charge of carrier, m^* is the effective mass, and τ is the relaxation time. The σ in terms of constant relaxation time as a function of temperature is depicted in Fig. 6(b). Due to the large band gap in the $R3m$ phase, it has less electrical conductivity compared to the $Fm3m$ and $Pm3m$ phases. The value of σ as a function of temperature remains constant in the whole range of temperature. According to Weidemann-Franz law, the electronic thermal conductivity, κ_e, is directly proportional to σ and depends on τ. It has been observed from Figs. 6(b) and 6(c) that the $R3m$-GeTe has a lower value of σ and κ_e compared to the $Fm3m$ and $Pm3m$-GeTe, which shows more thermal stability for $R3m$-GeTe compared to the $Fm3m$ and $Pm3m$ phases of GeTe. It is known that the waste of heat can be one of the most important renewable sources of energy as it can be converted into electricity by the Seebeck effect [54]. Therefore a great deal of attention is devoted to developing new thermoelectric materials. The efficiency of thermoelectric materials requires high thermoelectric power factor ($S^2\sigma$). However, for bulk materials, there are some restrictions to increase thermoelectric efficiency. The low carrier concentration required for high value of Seebeck coefficients results into low electrical conductivity, while a large electrical conductivity simultaneously increases electrical thermal conductivity. Figure 7 presents
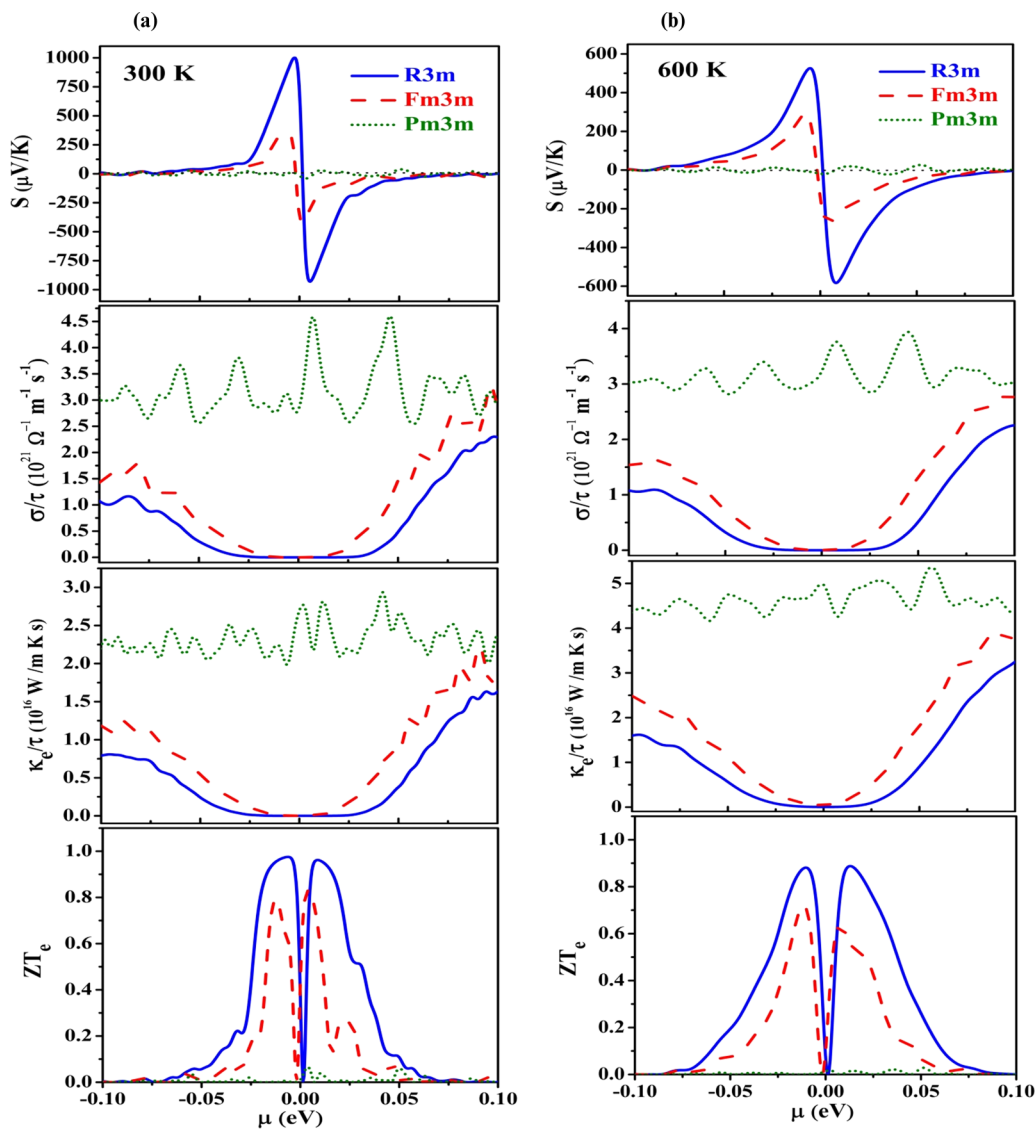
FIG. 7. Seebeck coefficient, electrical conductivity, electronic thermal conductivity, and ZT_e as a function of chemical potential (μ) for (a) 300 and (b) 600 K for all three $R3m$, $Fm3m$, and $Pm3m$ phases.

the chemical potential (μ) dependent transport coefficient for GeTe at temperatures 300 K (band a) and 600 K (band b). The positive value of μ corresponds to n-type doping with the Fermi level moving in the upward direction, while negative value of μ corresponds to p-type doping with the Fermi level moving in the downward direction. However, near the Fermi level, enhancement of Seebeck coefficient (S) results due to low n-type and p-type doping. The maximum value S is found for the rhombohedral phase with 993 μV/K, while for $Fm3m$ and $Pm3m$, it is 412 and 40 μV/K, respectively. The difference in S is clearly due to the electronic band gaps. However, at 600 K, this value becomes approximately half, 526 μV/K, for the rhombohedral phase. The larger value of Seebeck coefficient enhances the thermoelectric power factor. The electrical conductivity σ is almost independent of temperature, while κ_e increases slightly with temperature. As the metals have a very high electrical and electronic thermal conductivity, we get the higher value of σ and κ_e for $Pm3m$-GeTe, while $R3m$ and $Fm3m$-GeTe have lower value of σ and κ_e compared

to $Pm3m$ phase. The semiconducting nature of rhombohedral and $Fm3m$-GeTe results into the zero value of σ and κ_e at $\mu = 0$ eV.

In the last few years, there were several approaches focused on improving ZT such as utilization of quantum effects by using materials with complex superlatice or reducing the thermal conductivity by increasing the disorder [55–57]. However, increasing charge carriers can increase the Seebeck coefficient which results in low thermal conductivity [58]. ZT can be determined by the following expression [59]:

$$ZT = \frac{S^2 \sigma \mathrm{T}}{\kappa_e} \frac{\kappa_e}{\kappa_e + \kappa_{\mathrm{latt}}} = ZT_e \frac{\kappa_e}{\kappa_e + \kappa_{\mathrm{latt}}}. \quad (4)$$

The quantity $ZT_e = S^2 \sigma T / \kappa_e$ is now independent of relaxation time and ignores the lattice thermal conductivity. The ZT_e equal to 0.97 is highest for the rhombohedral GeTe, while $Fm3m$-GeTe exhibits a value of 0.82 at 300 K. This decreases to 0.88 and 0.71 for rhombohedral and $Fm3m$-GeTe, respectively, at 600 K. The behavior of ZT_e shown in Fig. 7 as
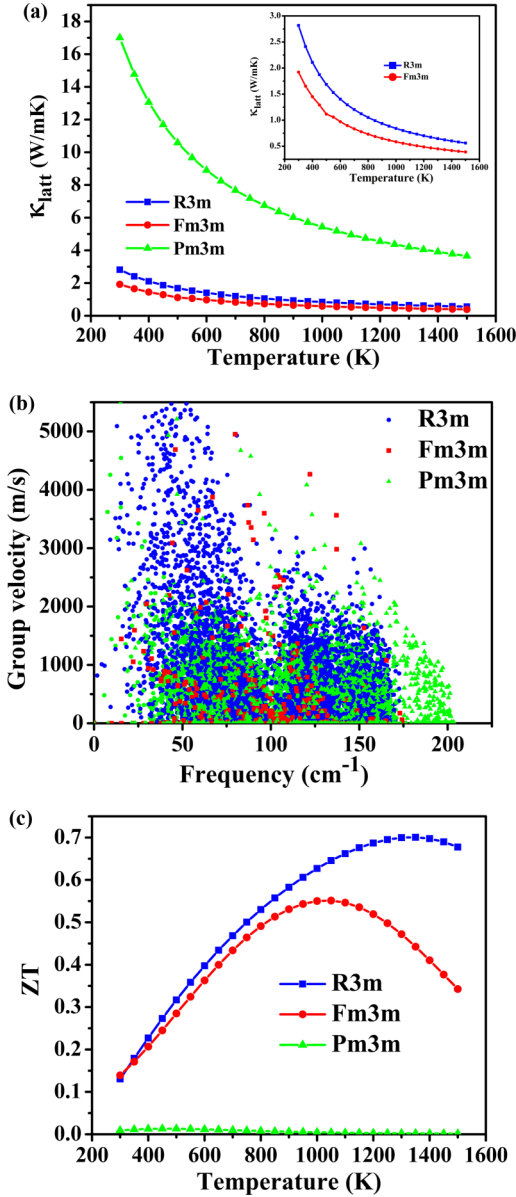
FIG. 8. (a) The lattice thermal conductivity (κ_{latt}), (b) group velocity, and (c) the figure of merit (*ZT*) as a function of temperature for all three phases.

a function of μ is also observed in GeSe and SnSe [59]. The difference in ZT_{e} between rhombohedral and $Fm3m$ is due to the lesser difference in their band gap. It is observed that the $Pm3m$-GeTe exhibits negligible value of ZT_{e} compared to the other two phases due to high thermal conductivity and lower Seebeck coefficient. The maximum value of ZT_{e} near the $\mu = 0$ eV region suggests lower *p*-type or *n*-type doping, which can drastically increase the thermoelectric performances. The temperature-dependent ZT_{e} presented in Fig. 6(d) shows that the $R3m$-GeTe has maximum value of ZT_{e} with 0.7 at 1300 K. Lower value of Seebeck coefficient and higher κ_{e} result in very lower value of ZT_{e} (∼0.1) in the $Pm3m$ phase.

The calculated temperature-dependent lattice thermal conductivity κ_{latt} of GeTe in all three phases is presented in Fig. 8(a). It is clearly seen that the GeTe in $R3m$ and $Fm3m$ phases depict lower value of κ_{latt} than the $Pm3m$ phase of GeTe

in the entire range of studied temperatures. There is a large difference in κ_{latt} between $Pm3m$ and other phases of GeTe in the entire temperature range. A strong coupling between acoustic and optical phonons is observed in the $Fm3m$ phase, while in $R3m$ phase, we observed a gap between acoustic and optical phonons, which results in the lower value of κ_{latt} in $Fm3m$-GeTe. Our calculated κ_{latt} of 2.81 W m^{-1} K^{-1} at 300 K for the $R3m$ phase has a good agreement with a previous report [48]. We also calculate the phonon-dependent group velocity presented in Fig. 8(b). We note that the $R3m$ phase of GeTe has higher group velocity compared to the $Fm3m$ phase of GeTe in the lower region of the frequency.

We calculated the thermoelectric figure of merit (*ZT*) with the contribution of Seebeck coefficient, electrical conductivity, and lattice thermal conductivity and presented the results in Fig. 8(c). We observe that at a higher temperature of about 1350 K the highest *ZT* of 0.7 is observed for $R3m$-GeTe, while at the same temperature it is 0.44 for $Fm3m$-GeTe. The $Pm3m$ phase of GeTe has a very low *ZT* value near zero in the entire temperature range. This study shows that $R3m$-GeTe can be used in high-temperature thermoelectric devices; however, due to the phase transition at 720 K, the $Fm3m$-GeTe phase will restrict the thermoelectric figure of merit. It is worth to mention that in this particular material, besides the standard strategy for *ZT* enhancement, phase stabilizing dopants is very promising approach, since at higher temperatures the $R3m$-GeTe is better.

IV. ELASTIC PROPERTIES

The calculation of elastic constants is important as they illustrate fundamental properties such as mechanical stability, stiffness, brittleness, ductility, etc. In addition, they also provide information about the anisotropic character of bonding. Therefore we have calculated the elastic constants of GeTe in $R3m$, $Fm3m$, and $Pm3m$ phases. There are three elastic constants C_{11}, C_{12}, and C_{44} for cubic symmetry, while for the rhombohedral phase there are six independent elastic components: C_{11}, C_{12}, C_{13}, C_{14}, C_{33}, and C_{44}. To satisfy the mechanical stability, a solid is required to satisfy the Born criteria. The Born criteria of mechanical stability in $R3m$ and cubic symmetries are given by Eqs. (5) and (6), respectively [60],

$$C_{11} > |C_{12}|; \ C_{44} > 0; \ C_{13}^2 < \tfrac{1}{2}C_{33}(C_{11} + C_{12});$$
$$C_{14}^2 < \tfrac{1}{2}C_{44}(C_{11} - C_{12}) = C_{44}C_{66}, \quad (5)$$

$$C_{11} > 0; \ C_{11} > C_{12}; \ C_{11} + 2C_{12} > 0. \quad (6)$$

The calculated elastic constants are listed in Table II, which shows that GeTe is mechanically stable for both symmetries. Table II also indicates the bulk modulus *B*, shear modulus *G*, and Young's modulus *Y* for $R3m$, $Fm3m$, and $Pm3m$ phases of GeTe calculated using the following expressions [43]:

$$B = \tfrac{1}{2}(B_V + B_R), G = \tfrac{1}{2}(G_V + G_R) \ Y = \frac{9BG}{3B + G}, \quad (7)$$

where B_V and B_R are the bulk modulus and G_V and G_R are the shear modulus calculated using the Voigt and Reuss approximations [61,62]. For the rhombohedral and $Fm3m$

TABLE II. Calculated elastic constant (C_{ij} in GPa), bulk modulus (B in GPa), shear modulus (G in GPa), Young's modulus (Y in GPa), anisotropic factor (A), Poisson's ratio (ν), Cauchy's pressure (C_p in GPa), and G/B ratio for $R3m$, $Fm3m$, and $Pm3m$ phases of GeTe at their respective stable pressure.

Elastic properties	$R3m$	$Fm3m$ (3.1 GPa)	$Pm3m$ (33 GPa)
C_{11}	92.0	168.2	309.8
C_{12}	16.3	13.5	137.8
C_{13}	20.5	–	–
C_{14}	17.5	–	–
C_{33}	44.5	–	–
C_{44}	33.1	21.3	107.6
C_{66}	37.9	–	–
B	36.31	65.07	195.16
G	28.16	36.39	98.16
Y	67.14	93.09	254.64
A	0.87	0.28	1.25
ν	0.19	0.26	0.28
C_p	–16.89	–7.80	30.20
G/B	0.76	0.57	0.50

phases of GeTe, the bulk modulus shows good agreement with available results [63,64]. The elastic modulus of the $Pm3m$ phase is very high compared to other phases indicating more resistivity towards the compression. According to Pugh's criteria, the ratio of G/B determines whether the material is ductile or brittle [65]. If the value of $G/B < 0.57$, then materials show ductile behavior and for brittleness the ratio of G/B must be greater than 0.57. Our calculated value of G/B for the $R3m$ phase is 0.76, which is greater than 0.57, indicating the brittleness character of the $R3m$-GeTe. For the $Pm3m$ phase, it is 0.50, which indicates that the GeTe in the $Pm3m$ phase is ductile at 33 GPa. The Poisson's ratio ν, which is listed in Table II, provides the information about compressibility of materials. If the ratio of bulk modulus to shear modulus becomes infinity, then $\nu = 0.5$ and the material become incompressible [66]. Our calculated ν shows that the rhombohedral phase is more compressible compared to $Fm3m$ and $Pm3m$ phases as ν is quite low for the $R3m$ phase. To measure the degree of anisotropy, we have calculated the Zener anisotropic factor A using the following formula [67]:

$$A = \frac{2C_{11} - C_{12}}{C_{44}}.$$

The value of A for the rhombohedral, $Fm3m$, and $Pm3m$ phases is listed in Table II, and it indicates that all three phases are elastically anisotropic. The Cauchy's pressure C_p gives the information about bonding, ductility, and metallic behaviors of materials. The negative value of C_p for the rhombohedral and $Fm3m$ phases demonstrates brittleness, and a positive value of C_p reveals the ductile and metallic behavior of the $Pm3m$ phase of GeTe. This agrees with the G/B ratio and DOS of the $Pm3m$ phase.

V. CONCLUSIONS

We have investigated the structural, dynamical, mechanical, and thermoelectric properties of GeTe in $R3m$, $Fm3m$, and $Pm3m$ phases using density functional theory and Boltzmann transport equations. Our study reports that the GeTe exists in the $R3m$ phase at ambient conditions, while the $Fm3m$ and $Pm3m$ phases are dynamically stable at 3.1 and 33 GPa, respectively. The $R3m$ phase of GeTe shows semiconducting behavior with a 0.66 eV direct band gap, while the $Pm3m$ phase of GeTe exists in a metallic state at stable conditions. The calculation shows that the $R3m$ and $Fm3m$ phases of GeTe have the lowest thermal conductivity among all three phases. The analysis of thermoelectric properties shows that the rhombohedral phase of GeTe shows better thermoelectric performance among all three considered phases of GeTe, however, due to phase transition at 720 K, restricts the thermoelectric figure of merit to the $Fm3m$-GeTe value for higher temperatures. Thus we have pointed out that research on rhombohedral phase stabilization enables a very promising strategy for ZT enhancement in GeTe. The $R3m$-GeTe emerges as an efficient thermoelectric material for high-temperature thermoelectric applications, with $ZT_{max} = 0.7$ at 1350 K. The elastic analysis shows that all three phases follow the Born stability criteria and the Cauchy's pressure like DOS show that the $Pm3m$ phase is metallic.

[1] S. Ovshinsky, Phys. Rev. Lett. **21**, 1450 (1968).

[2] M. Libera and M. Chen, J. Appl. Phys. **73**, 2272 (1993).

[3] R. Shaltaf, E. Durgun, J. Y. Raty, Ph. Ghosez and X. Gonze, Phys. Rev. B **78**, 205203 (2008).

[4] N. Ya. Fogel, E. I. Buchstab, Yu. V. Bomze, O. I. Yuzephovich, A. Yu. Sipatov, E. A. Pashitskii, A. Danilov, V. Langer, R. I. Shekhter, and M. Jonson, Phys. Rev. B **66**, 174513 (2002).

[5] Y. Matsushita, H. Bluhm, T. H. Geballe, and I. R. Fisher, Phys. Rev. Lett. **94**, 157002 (2005).

[6] R. A. Hein, J. W. Gibson, R. Mazelsky, R. C. Miller, and J. K. Hulm, Phys. Rev. Lett. **12**, 320 (1964).

[7] G. S. Do, J. Kim, S. H. Jhi, C. H. Park, S. G. Louie, and M. L. Cohen, Phys. Rev. B **82**, 054121 (2010).

[8] A. K. Singh and R. G. Hennig, Appl. Phys. Lett. **105**, 042103 (2014).

[9] R. Fei, W. Li, J. Li, and L. Yang, Appl. Phys. Lett. **107**, 173104 (2015).

[10] L. Xu, H. Q. Wang and J. C. Zheng, J. Electron. Mater. **40**, 641 (2011).

[11] S. Perumal, S. Roychowdhury, and K. Biswas, J. Mater. Chem. C **4**, 7520 (2016).

[12] T. Chattopadhyay, A. Werner, and H. G. von Schnering, in *High Pressure in Science and Technology*, edited by C. Homan, R. K. MacCrone, and E. Whalley, MRS Symposia Proceedings No. 22, (Materials Research Society, Pittsburgh, 1984), p. 83.

[13] Y. Fujii, K. Kitamura, A. Onodera, and Y. Yamada, Solid State Commun. **49**, 135 (1984).

[14] T. Chattopadhyay, H. G. von Schnering, W. A. Grosshaus, and W. B. Holzapfel, Physica B & C **139-140**, 356 (1986).

[15] A. Onodera, Y. Fujii, and S. Sugai, Physica B & C **139-140**, 240 (1986).

[16] N. R. Serebryanaya, V. D. Blank, and V. A. Ivdenko, Phys. Lett. A **197**, 63 (1995).

[17] H. Wiedemeier and P. A. Siemers, Z. Anorg. Allg. Chem. **431**, 299 (1977).

[18] T. Chattopadhyay, J. X. Boucherle, and H. G. von Schnering, J. Phys. C **20**, 1431 (1987).

[19] E. F. Steigmeier and G. Harbeke, Solid State Commun. **8**, 1275 (1970).

[20] D. D. Vaughn, D. Sun, S. M. Levin, A. J. Biacchi, T. S. Mayer, and R. E. Schaak, Chem. Mater. **24**, 3643 (2012).

[21] L. Makinistian and E. A. Albanesi, J. Phys. Condens. Matter **19**, 186211 (2007).

[22] A. Onodera, I. Sakamoto, Y. Fujii, N. Môri, and S. Sugai, Phys. Rev. B **56**, 7935 (1997).

[23] K. Jeong, S. Park, D. Park, M. Ahn, J. Han, W. Yang, H. S. Jeong and M. H. Cho, Sci. Rep. **7**, 955 (2017).

[24] H. Alam and S. Ramakrishna, Nano Energy **2**, 190 (2013).

[25] Y. Gelbstein, O. B. Yehuda, E. Pinhas, T. Edrei, Y. Yadia, Z. Dashevsky, and M. P. Dariel, J. Electron. Mater. **38**, 1478 (2009).

[26] Di Wu, L. Zhao, S. Hao, Q. Jiang, F. Zheng, J. W. Doak, H. Wu, H. Chi, Y. Gelbstein, C. Uher, C. Wolverton, M. Kanatzidis, and J. He, J. Am. Chem. Soc. **136**, 11412 (2014).

[27] J. Li, Z. Chen, X. Zhang, Y. Sun, J. Yang and Y. Pei, NPG Asia Mater. **9**, e353 (2017).

[28] P. Giannozzi, S. Baroni, N. Bonini, M. Calandra, R. Car, C. Cavazzoni, D. Ceresoli, G. L. Chiarotti, M. Cococcioni, I. Dabo, A. Dal Corso, S. Fabris, G. Fratesi, S. de Gironcoli, R. Gebauer, U. Gerstmann, C. Gougoussis, A. Kokalj, M. Lazzeri, L. Martin-Samos, N. Marzari, F. Mauri, R. Mazzarello, S. Paolini, A. Pasquarello, L. Paulatto, C. Sbraccia, S. Scandolo, G. Sclauzero, A. P. Seitsonen, A. Smogunov, P. Umari, and R. M. Wentzcovitch, J. Phys.: Condens. Matter **21**, 395502 (2009).

[29] C. G. Broyden, IMA J. Appl. Math. **6**, 76 (1970).

[30] R. Fletcher, Comput. J. **13**, 317 (1970).

[31] D. G. Goldfarb, Math. Comp. **24**, 23 (1970).

[32] D. F. Shanno, Math. Comp. **24**, 647 (1970).

[33] S. D. Gupta and P. K. Jha, Earth Planet. Sci. Lett. **401**, 31 (2014).

[34] J. P. Perdew, K. Burke, and M. Ernzerhof, Phys. Rev. Lett. **77**, 3865 (1996).

[35] N. Troullier and J. L. Martins, Phys. Rev. B **43**, 1993 (1991).

[36] G.-D. Lee, M. H. Lee and J. Ihm, Phys. Rev. B **52**, 1459 (1995).

[37] S. Baroni, S. de Gironcoli, A. Dal Corse and P. Giannozzi, Rev. Mod. Phys. **73**, 515 (2001).

[38] G. K. H. Madsen and D. J. Singh, Comput. Phys. Commun. **175**, 67 (2006).

[39] A. Shafique and Y.-H. Shin, Sci. Rep. **7**, 506 (2017).

[40] X.-M. Wang, D.-C. Mo, and S.-S. Lu, J. Chem. Phys. **138**, 204704 (2013).

[41] W. Li, J. Carrete, N. A. Katcho, and N. Mingo, Comput. Phys. Commun. **185**, 1747 (2014).

[42] R. Golesorkhtabar, P. Pavone, J. Spitaler, P. Pusching and C. Draxl, Comp. Phys. Commun. **184**, 1861 (2013).

[43] R. Hill, Proc. Phys. Soc. **65**, 349 (1952).

[44] S. S. Kabalkina, L. F. Vereshchagin, and N. R. Serebryanaya, Sov. Phys. JETP **24**, 917 (1967).

[45] See Supplemental Material at http://link.aps.org/supplemental/10.1103/PhysRevB.97.134105 for intermediate structures and Energy versus Volume graph.

[46] B. Pereira, I. Sergueev, S. Gorsse, J. Dadda, E. Müller, and R. P. Hermann, Phys. Status Solidi B **250**, 1300 (2013).

[47] T. Nonaka, G. Ohbayashi, Y. Toriumi, Y. Mori and H. Hashimoto, Thin Solid Films **370**, 258 (2000).

[48] D. Campi, L. Paulatto, G. Fugallo, F. Mauri and M. Bernasconi, Phys. Rev. B **95**, 024311 (2017).

[49] G. Yumnam, T. Pandey and A. K. Singh, J. Chem. Phys. **143**, 234704 (2015).

[50] L. Zhang, M.-H. Du, and D. J. Singh, Phys. Rev. B **81**, 075117 (2010).

[51] M. Cohen, Phys. Rev. **121**, 387 (1961).

[52] K. M. Rabe and J. D. Joannopoulos, Phys. Rev. B **36**, 3319 (1987).

[53] N. F. Hinsche, B. Y. Yavorsky, M. Gradhand, M. Czerner, M. Winkler, J. Konig, H. Bottner, I. Mertig and P. Zahn, Phys. Rev. B **86**, 085323 (2012).

[54] F. J. DiSalvo, Sci. **285**, 703 (1999).

[55] J.C. Zheng, Front. Phys. China **3**, 269 (2008).

[56] L.E. Bell, Science **321**, 1457 (2009).

[57] Y. Zhang, X. Ke, C. Chen, J. Yang, and P.R.C. Kent, Phys. Rev. B **80**, 024304 (2009).

[58] H. Ohta, S. Kim, Y. Mune, T. Mizoguchi, K. Nomura, S. Ohta, T. Nomura, Y. Nakanishi, Y. Ikuhara, M. Hirano, H. Hosono and K. Koumoto, Nat. Mater. **6**, 129 (2007).

[59] G. Ding, G. Gao and K. Yao, Sci. Rep. **5**, 9567 (2017).

[60] F. Mouhat and F. X. Coudert, Phys. Rev. B **90**, 224104 (2014).

[61] W. Voigt, *Lehrbuch der Kristallphysik (mit Ausschluss der Kristalloptik)* (B. G. Teubner Verlag, Leipzig, Berlin, 1928).

[62] A. Reuss, Z. angew. Math. Mech. **9**, 49 (1929).

[63] A. Ciucivara, B. R. Sahu, and L. Kleinman, Phys. Rev. B **73**, 214105 (2006).

[64] S. Palaz, H. Koc, A. M. Mamedov and E. Ozbay, IOP Conf. Ser.: Mater. Sci. Eng. **175**, 012004 (2017).

[65] S. F. Pugh, Philos. Mag. **45**, 823 (1954).

[66] P. H. Mott, J. R. Dorgan and C. M. Roland, J. Sound Vibr. **312**, 572 (2008).

[67] C. Zener, *Elasticity and Anelasticity of Metals* (University of Chicago Press, Chicago, 1948).